Simultaneous Transmission-Emission Thallium-201 Cardiac SPECT: Effect of Attenuation Correction on Myocardial Tracer Distribution

Edward P. Ficaro, Jeffrey A. Fessler, Robert J. Ackermann, W. Leslie Rogers, James R. Corbett and Markus Schwaiger

Division of Nuclear Medicine, Department of Internal Medicine, The University of Michigan Medical Center, Ann Arbor, Michigan

This study evaluates the effect of attenuation correction on regional myocardial tracer distributions defined by ^{201}Tl cardiac perfusion SPECT images obtained from healthy volunteers and patients with coronary heart disease. **Methods:** A three-detector SPECT system equipped with an ^{241}Am line source and a fan-beam collimator was used for simultaneous transmission/emission (^{201}Tl) tomography on 40 patients and 10 normal volunteers. Uncorrected emission images were reconstructed using filtered backprojection (FBP), whereas the attenuation corrected images were iteratively reconstructed with a regularized, least-squares algorithm utilizing the attenuation map computed from the transmission data. Both sets of images were reoriented into short-axis and vertical long-axis slices. Circumferential profile analysis was applied to both datasets of short-axis slices. **Results:** The normal volunteers demonstrated improved homogeneity in tracer distribution. For a basal short-axis slice, the lateral-to-posterior activity ratio improved from 1.17 ± 0.12 for FBP to 1.01 ± 0.07. Basal attenuation appeared properly compensated as the peak basal-to-apical slice activity gradient along the posterior-inferior wall changed from 1.15 ± 0.12 for FBP to 1.01 ± 0.09. The apex of the attenuation corrected images showed a significant decrease in activity relative to the base which appeared consistent with anatomic wall thinning. For the inferior and basal septal regions, the defect severity was slightly less in the attenuation corrected images, but the defects were more sharply defined compared to the FBP image defects. **Conclusion:** These results indicate that attenuation correction is clinically feasible and accurately corrects for photon attenuation. Clinical validation, however, is necessary to define the diagnostic benefits.

Key Words: transmission tomography; single-photon emission computed tomography; coronary artery disease; attenuation correction; cardiac imaging

J Nucl Med 1995; 36:921–931

In cardiac SPECT, artifactual abnormalities of regional tracer distribution in the myocardium result from photon attenuation in the chest. Since the structures within the thorax differ greatly in density (e.g., bone, tissue, lung), conventional attenuation correction algorithms assuming uniform attenuation are not applicable (*1*). As a result, several approaches have been described using conventional SPECT imaging systems for performing transmission computed tomography (TCT) in an effort to directly measure the nonuniform density maps of the thorax (*2–15*). Measured attenuation maps can be used to iteratively reconstruct the measured emission projection data to compensate for inhomogeneous photon attenuation in the chest.

Initial attenuation correction systems (*3–5*) incorporated an uncollimated ^{99m}Tc flood source attached opposite a detector fitted with a parallel-hole collimator. To eliminate photon crosstalk between the emission and transmission windows, the TCT scan was obtained prior to radiotracer injection. This system had several disadvantages. The sequential imaging protocol increased patient imaging time, thereby increasing the probability of patient motion and misregistration of the emission and transmission datasets. Misalignment between the emission and transmission data will introduce errors into the attenuation corrected images. The second problem associated with this geometry was that the uncollimated flood source had a large photon flux component not directed inline with the parallel collimation of the detector. Consequently, this geometry has low sensitivity, the highest radiation dose to the patient and attenuation maps that have poor resolution and measure broad beam not narrow beam attenuation coefficients. The key advantage of this geometry was that the imaging field of view (FOV) was equal to the width of the detector (typically 40 cm).

To decrease patient imaging time and eliminate possible patient movement between the TCT and SPECT scans, the TCT and SPECT data may be acquired simultaneously. A consequence of simultaneous acquisition using dual-energy windows is photon crosstalk occurring between the transmission and emission windows. To minimize crosstalk in

Received May 10, 1994; revision accepted Oct. 24, 1994.
For correspondence or reprints contact: Edward Ficaro, PhD, The University of Michigan Hospitals B1G412/0028, 1500 E. Medical Center Dr., Ann Arbor, MI 48109.

the count-poor emission data, the photon energy of the transmission isotope was chosen to be less than the emission photon energy. For ^{99m}Tc radiotracers (140 keV photons), Bailey et al. used a ^{153}Gd transmission source (*6*) (97 and 103 keV photons). For ^{201}Tl radiotracers, Frey et al. chose ^{99m}Tc due to its availability and because initial attempts at finding a radioisotope with an energy less than the 75 keV photopeak of ^{201}Tl were unproductive (*7*). In a recent article, we proposed the use of ^{241}Am (60 keV photons) for the transmission source (*14*). This isotope can be used with both radiotracers and introduces the least amount of contamination to the emission data; however, despite the prudent choice of transmission isotope, simultaneous TCT/SPECT acquisitions with a single detector do not permit direct measurement of the energy window crosstalk. As a result, the removal of crosstalk requires empirical estimations which introduce bias into the measured transmission and emission data.

To improve the sensitivity in the TCT and SPECT measurements, Manglos et al. performed TCT measurements using a ^{99m}Tc point source opposite a conebeam collimator (*8,9*). With this geometry, there was a significant increase in resolution in the attenuation maps which now measured narrow beam attenuation coefficients. The disadvantage of this system derives from the inherent magnification of conebeam collimators which produce truncated projection data. Due to the incompleteness of the projection data, conventional filtered backprojection algorithms produced a ring artifact around the imaging FOV which render these algorithms clinically unusable. As a result, iterative reconstruction techniques are required to fill in the truncated regions of the image at an increase in computation time.

Tung, Gullberg and associates (*11*) used a three-detector SPECT system with a collimated line source opposite a detector fitted with a 65-cm fanbeam collimator to perform simultaneous TCT/SPECT. Provided the projection data are collected in the transmission and emission windows over 360°, this system directly measures the crosstalk in the transmission window from emission photons and minimizes bias in the corrected transmission data. Similar to the conebeam collimator, the limitation of this system was the inherent magnification of the fanbeam collimator which truncates the transmission projection data. Although longer focal length collimators would decrease the degree of truncation, the orbit radii of the two emission detectors would have to be increased to prevent attenuation of the edges of the transmission photon beam. Since resolution of the emission data degrades as the orbit radius is increased, this tradeoff is not advantageous. It was determined that a focal length of 65 cm minimized truncation when using patient contoured orbits.

Jaszczak et al. utilized the same TCT/SPECT geometry and increased the focal length of the fanbeam collimator from 65 to 110 cm and proposed a fast TCT scan (1–2 min) prior to the SPECT scan (*12*). The increased focal length of the collimator increased the diameter of the transmission imaging FOV to 31 cm compared to 25 cm for the 65-cm collimator (diameters based on a 22-cm orbit radius). To acquire sufficient counting statistics during the short duration TCT scan, this system used a 3.33 GBq (90 mCi) ^{99m}Tc line transmission source. By shielding the transmission source during the SPECT scan, crosstalk contamination in the emission data was eliminated and an estimate of the crosstalk component in the transmission data was possible. The disadvantages of this system were the sequential acquisition and the high photon flux of the transmission line source. Although the TCT scan was short in duration, misalignment errors between the TCT and SPECT images due to patient motion can still occur. The high photon flux of the transmission source can produce count rates exceeding the deadtime of the detector, especially if the patient does not fill the entire FOV. If deadtime can be kept constant and equal to the reference scan in air, its effects can be minimized. If, however, the deadtime varies as a function of projection angle and is not equal to the deadtime of the reference scan, the transmission images will have artifacts and will provide inaccurate estimates of patient attenuation.

A scanning line source opposite a parallel-hole collimator is another solution to truncation and crosstalk problems (*13*). The advantages of this system are: (1) direct measurement of transmission-emission crosstalk using sophisticated electronic masking of the imaging area based on position of the source and (2) minimal truncation in transmission data due to the parallel-hole collimator. The disadvantage of this system is an increase in patient imaging time because the transmission and emission data are acquired not simultaneously, but sequentially in an alternating, interleaved fashion. To minimize the increase in patient imaging time, the transmission acquisition time is reduced, resulting in noisier attenuation maps. Although a stronger source can be used, as proposed in the fast TCT system, deadtime effects from the transmission source in this system affect both the emission data and the crosstalk estimates. In addition, this system requires the most stringent quality assurance testing to ensure that the sophisticated electronic masking hardware is operating coincidentally with the translating transmission source.

A new TCT/SPECT geometry has been reported that allows simultaneous acquisitions while minimizing image truncation (*15*). In this system, a line source is positioned opposite an offset fanbeam collimator (the focal line is offset laterally from the center of the collimator). On a triple-detector system, the line source is attached to the edge of one of the collimators and the offset fanbeam collimator is attached to an opposite detector. To maintain the source-to-collimator focal length geometry, the radii of the source and offset fanbeam detectors are fixed at 28.4 and 24.4 cm, respectively. This geometry provides a transmission imaging FOV diameter of 37 cm (for a 40-cm wide detector). The disadvantage of this system is variation both in emission image resolution as measured by each of the three detectors since each have different orbit radii. Additionally, there is partial masking of the detector to which

the source is attached. As a result, the projection data cannot be combined prior to reconstruction but must be properly weighted (depth-dependent) to minimize image resolution degradation and distortion during the reconstruction.

We chose to use a multidetector SPECT system with a ^{241}Am line source and a 65-cm fanbeam collimator. This decision was based on the following considerations: (1) the ability of a multidetector system to directly measure the emission crosstalk in the transmission data to provide unbiased crosstalk compensation, (2) the photon energy of the ^{241}Am transmission photons (60 keV) is less than the emission photon energies of both ^{201}Tl and ^{99m}Tc tracers which minimize contamination of the emission tracer data (*14*), (3) true simultaneous TCT/SPECT acquisitions are possible and (4) line source and fanbeam collimators are commercially available. By using this system, we evaluated the effect of attenuation correction on tracer distribution in the myocardium of healthy volunteers and patients with coronary heart disease. Phantom studies (with and without defects) were performed to validate the acquisition and processing techniques and to provide reference measurements for the patient data. Attenuation-Corrected and uncorrected ^{201}Tl myocardial tracer distributions were compared in normals and in patients with coronary heart disease and defined tracer distribution defects.

MATERIALS AND METHODS

Imaging System

To perform simultaneous TCT/SPECT imaging, a collimated line source holder was attached to the rotating gantry of the PRISM 3000 SPECT imaging system (Ohio Imaging of Picker International, Bedford Heights, OH). The source holder was positioned opposite and parallel to one of the three detectors (detector 1). This detector was fitted with a low-energy, general-purpose, fanbeam collimator with a focal length of 65 cm (Fig. 1). The transmission source consisted of a 5.55 GBq (150 mCi) ^{241}Am line source (Isotope Products Laboratories, Burbank, CA) sealed in a 0.3-mm thick stainless steel tube with an active volume of 2.4 mm i.d × 240 mm. The line source was radially collimated to a 50° fanbeam and axially collimated with 50.8 × 25.4 × 0.25 mm strips of lead foil separated by 3.2 mm thick foam spacers. Detectors 2 and 3 were fitted with low-energy, high-resolution, parallel-hole collimators.

Transmission and emission projection data were acquired in 64 × 64 matrices for all detectors. Projections were acquired in 6° steps over a 360° circular orbit for 16 sec per step for a total scan time of 16 min. An energy window of 59.0 ± 5.9 keV was used for the ^{241}Am transmission photons. Typical transmission count rates ranged from 6 to 30 kcps, depending on patient size, positioning and density. Two energy windows, one at 74.0 ± 9.25 keV and the other at 167 ± 12.5 keV, were summed to record ^{201}Tl emission data. The typical ^{201}Tl count rate for the patient studies was 1.53 ± 0.35 kcps. The projection data from the three detectors were acquired simultaneously in both the transmission and the summed ^{201}Tl emission windows. A 20-min transmission "blank" scan (approximately 30 million counts) was acquired to compute attenuation line length sinograms from the transmission data. To minimize deadtime effects during the blank scan, the source was shielded with a curved lead shield with a uniform thickness of 0.76 mm to reduce the beam intensity by 97%.

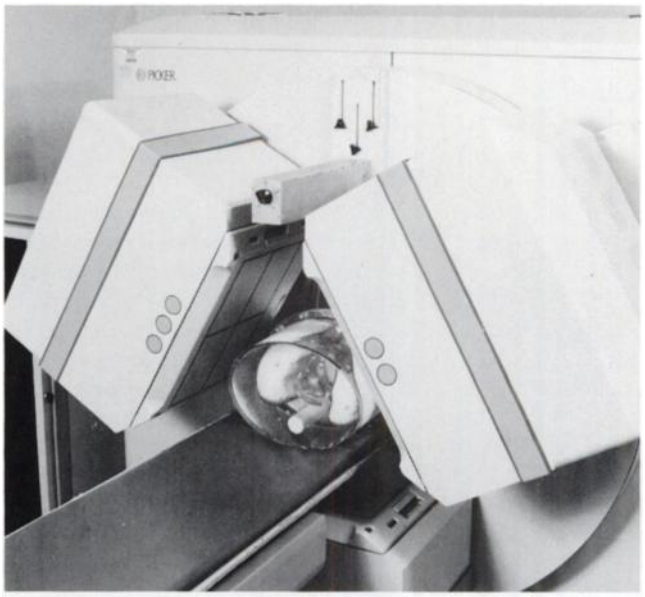

FIGURE 1. Imaging system used to perform simultaneous transmission-emission tomography. Detector 1, fitted with a fanbeam collimator and collecting transmission and emission data, is located beneath the table. Detectors 2 and 3 are fitted with parallel-hole collimators and measure uncontaminated emission projection data.

Phantom Studies

Phantom studies were performed using an elliptical cylinder (31 × 27 cm) with lung, spine and cardiac inserts (Data Spectrum Corp., Chapel Hill, NC). The lung inserts consisted of a mixture of foam beads and water providing a lung density of 0.4 g/cm^3. The heart chamber was filled with 56 kBq/ml and the body and lungs were filled with 11 kBq/ml ^{201}Tl to simulate an injection of 111 MBq (3 mCi) ^{201}Tl with 6% uptake in the myocardium and thorax with a heart-to-background ratio of 5:1. A baseline/normal study was acquired without defects in the chamber wall. To investigate the regional effects of attenuation and attenuation compensation on defect severity and extent, a 2-cm × 45° cold defect was placed in the basal portion of the "myocardial" wall and transmission and emission images were acquired. The defect was placed in the anterior, lateral, posterior and septal positions.

Patient Studies

The patient studies consisted of healthy volunteers (n = 10) with no previous history of heart disease and coronary heart disease patients (n = 40) from the clinic population. Each patient underwent an adenosine stress study followed by a reinjection-redistribution study 4 hr later. The adenosine was infused over 6 min at 0.140 mg/kg/min using a Harvard pump. Three min after the start of the adenosine infusion, 111 MBq (3 mCi) of thallous chloride were injected intravenously. Imaging began within 15 min. For the delayed study, the patient was reinjected with 1 mCi thallous chloride approximately 15 min before reimaging.

Five of the coronary heart disease patients imaged with this protocol were selected for presentation to illustrate the effects of attenuation correction on defect severity and extent in relation to defect position within the myocardium. In addition, the elliptical constraint for the body outline required by the transmission reconstruction algorithm will be given for each patient along with an

estimate of the patient's attenuation map that is truncated due to the TCT imaging geometry.

Data Processing

Reconstructed Attenuation Maps. Prior to reconstructing the attenuation maps, the ^{201}Tl crosstalk in the transmission projection data was removed by transforming the ^{201}Tl crosstalk projection data in detector 2 (data collected in ^{241}Am window) from parallel to fanbeam geometry and subtracting this from the transmission projections of detector 1. Pixels with negative or zero counts were assigned a value based on a weighted average of its neighbors. Attenuation line length sinograms were computed from the natural log of the ratio of blank to measured transmission counts and were input to the iterative reconstruction process.

Due to the inherent magnification of the fanbeam collimator, the transmission data were truncated for the phantom and patient studies. Conventional filtered backprojection (FBP) was incapable of estimating the undersampled regions in the image and subsequently a ring artifact was produced. For this reason, iterative reconstruction techniques were employed (*16*). Based on simulation reconstructions (*17*), we chose a weighted least squares algorithm that minimizes the following objective function (*18,19*):

$$\Phi(\mu) = \tfrac{1}{2}(\mathbf{y} - \mathbf{A}\mu)'\mathrm{Diag}\{\sigma^{-2}\}(\mathbf{y} - \mathbf{A}\mu) + \beta\tfrac{1}{2}\sum_{j}\sum_{k\in N_j} w_{jk}\tfrac{1}{2}(\mu_j - \mu_k)^2, \quad \text{Eq. 1}$$

where $\mathbf{y}$ is attenuation line length sinogram, σ^{-2} is the inverse variance of $\mathbf{y}$, $\mathbf{A}$ is the system geometric response matrix, and μ is the image of linear attenuation coefficient to be determined. During the reconstruction, a non-negativity constraint is imposed on μ. The second term in Equation 1 acts as a smoothing penalty (β is user-defined) which regularizes the ill-posed reconstruction. The weights w_{jk} are 1 for horizontal and vertical neighbors and $1/\sqrt{2}$ for diagonal neighbors. N_j represents the nearest eight neighbors.

Since the convergence rate of the algorithm depends on the initial estimate of μ, we construct an initial estimate using the following automated process. An image is reconstructed using FBP, and the truncation ring artifact is removed by zeroing all pixels outside of the nontruncated imaging area. From the camera orbit and table position, an estimate of the patient outline is made and inscribed on the FBP image. The area between the truncation and patient boundaries is then assigned the attenuation coefficient of tissue. Finally, the imaging table is added to the image to produce the initial estimate for Equation 1. The reconstruction is constrained by the outline of the patient and the imaging table.

With the initial image estimate, transaxial attenuation maps were reconstructed using 16 iterations of a cyclic coordinate descent algorithm (*18,19*) that minimizes Equation 1 with $\beta = 2^{16}$. A cutoff of 16 iterations was based on root mean square error analysis involving simulation and phantom studies. The average processing time for 18 slices was approximately 4 min. The attenuation maps were then scaled to a photon energy of 75 keV using

$$\mu_t(75\text{ keV}) = \frac{\mu_t^{tis}(75\text{ keV})}{\mu_t^{tis}(60\text{ keV})}\mu_t(60\text{ keV}), \quad \text{Eq. 2}$$

where $\mu_t(75\text{ keV})$ and $\mu_t(60\text{ keV})$ are the linear attenuation coefficients of tissue(tis) for the ^{201}Tl and ^{241}Am photons, respectively. In this work, we have used $\mu_t^{tis}(75\text{ keV}) = 0.183/\text{cm}$ for ^{201}Tl emission photons and $\mu_t^{tis}(60\text{ keV}) = 0.197/\text{cm}$ for ^{241}Am transmission photons, respectively (*19*). Although Equation 2 will overestimate linear attenuation of bone at 75 keV based on the 60 keV measurement (*14*), simulations have shown this effect to be insignificant for the work presented in this paper.

Attenuation-Corrected Emission Images. Prior to reconstructing the emission data, the uncontaminated emission data from detectors 2 and 3 were summed, and the emission data from detector 1 was corrected for contamination from ^{241}Am transmission photons (*14*). The corrected emission data from detector 1 was then converted from fanbeam to parallel-hole geometry and summed with the parallel data from detectors 2 and 3.

For the attenuation-corrected emission reconstruction, the following objective function was minimized,

$$\Phi(\lambda) = \tfrac{1}{2}(\mathbf{y} - \mathbf{F}\lambda)'\mathrm{Diag}\{\sigma^{-2}\}(\mathbf{y} - \mathbf{F}\lambda) + \beta\tfrac{1}{2}\sum_{j}\sum_{k\in N_j} w_{jk}\tfrac{1}{2}(\lambda_j - \lambda_k)^2, \quad \text{Eq. 3}$$

where $\mathbf{y}$ is emission sinogram, σ^{-2} is the inverse variance of $\mathbf{y}$, $\mathbf{F} = \mathbf{A} \cdot \mathbf{B}$ is the system response matrix accounting for geometry ($\mathbf{A}$) and photon attenuation ($\mathbf{B}$) and λ is the radiotracer activity concentration coefficient to be determined. The initial estimate to this objective function was a first-order Chang-corrected FBP image. From this estimate, transaxial emission images were reconstructed using eight iterations of Equation 3 with $\beta = 2^{-13}$. The average processing time for 18 slices was approximately 2 min.

The smoothness penalty used in reconstructing the emission images was chosen to yield resolution similar to a FBP reconstruction with a ramp filter with cutoff f_n (f_n = Nyquist frequency). To make this assessment, reconstructed FWHM measurements were made with a 20-cm od. cylinder filled with water containing three ^{99m}Tc filled line sources ({x, y} reference coordinates from center: {0, 0}, {8 cm, 0}, and {0, 8 cm}). Acquisition was performed with a circular orbit with a radius of 15 cm. For the central line source, the reconstructed FWHM were 11.8 and 12.0 mm for the FBP and attenuation-corrected reconstructed images, respectively. For a line source at the edge of the cylinder, the reconstructed resolution was 10.9 (tangential) and 7.75 mm (radial) for FBP and 10.1 (tangential) and 7.67 mm (radial) for the attenuation corrected image.

Uncorrected Emission Images. Emission images were reconstructed from 360° of projection data using conventional FBP with a ramp filter having a cutoff of f_n. Negative image pixels were not zeroed.

Image Processing and Display. Prior to reslicing, the FBP and attenuation-corrected images were filtered postreconstruction using a three-dimensional Butterworth filter of order 5 with a frequency cutoff of $0.6*f_n$. Uncorrected and attenuation-corrected emission images were resliced along the same short and vertical long axes. Polar map activity distributions were computed for the defect-free phantom and the normal volunteer studies. The circumferential sampling used in constructing the polar maps followed the methods of Garcia et al. (*21*). Unlike polar maps where each slice profile is normalized individually to 100%, the maps in this study were normalized to 100% as a whole. For the phantom and patient defect studies, circumferential profiles were computed from the short-axis slice through the center of the defect. In normalizing the FBP and attenuation-corrected circumferential profiles, the maximum profile value averaged over a 30° segment (5 points) in the FBP profile was determined and set to 100%. The attenuation-corrected profile was then normalized using the same angular range.

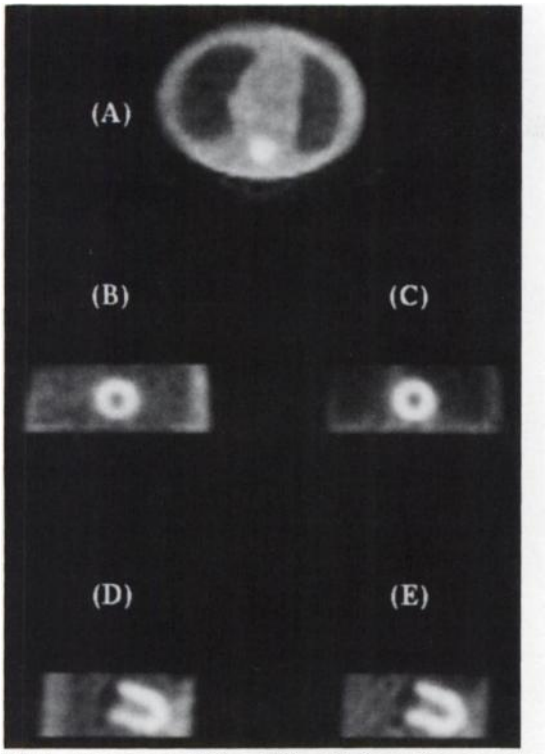

FIGURE 2. Uncorrected (B and D) and attenuation-corrected (C and E) reconstructed images from an anthropomorphic chest phantom with no defects present in the heart wall. The reconstructed attenuation map used to correct the emission data for photon attenuation is displayed in (A). The decreased activity in the inferior wall resulting from photon attenuation is evident in the uncorrected vertical long axis compared to the attenuation-corrected images.

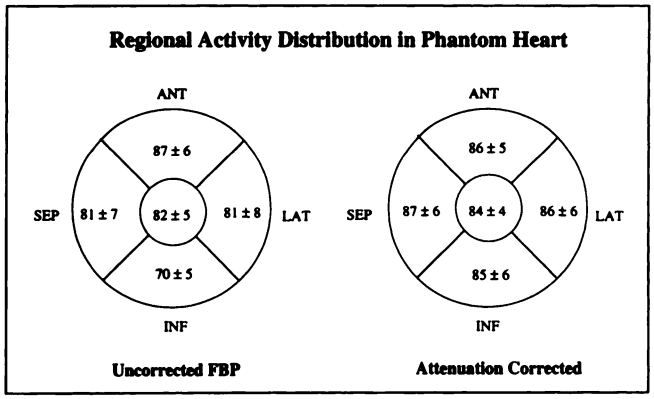

FIGURE 3. Polar map activity distribution in the heart wall (no defects) of an anthropomorphic chest phantom. The attenuation-corrected distribution shows improved homogeneity in activity compared to the uncorrected distribution. The maps were normalized to the percent maximal activity in the heart wall.

RESULTS

From the phantom measurements without defects, FBP and attenuation-corrected short- and long-axis slices are presented in Figure 2 and the polar maps are displayed in Figure 3. The heart wall of the chest phantom is uniform in thickness from base to apex and is expected to be uniform in activity distribution. The attenuation-corrected short-axis images showed the expected uniform activity distribution from base to apex. Conversely, the uncorrected FBP short-axis images were not uniform in activity (anterior-posterior ratio = 1.24), and the long-axis slices exhibited an activity gradient of 0.84 from base to apex in the posterior segment. In a comparison of heart-to-lung ratios, the ratio from the attenuation-corrected images (4.7:1) was in better agreement with the injected activity ratio (5:1) when compared to the FBP images (2.0:1).

From the phantom data acquired with a 2-cm × 45° cold defect, the polar maps were constructed from both uncorrected FBP and attenuation-corrected images with the defect in the lateral, anterior, septal and posterior positions (Fig. 4). Both sets of polar maps were normalized to the maximal activity in the entire heart wall. To quantify differences in defect severity (minimum percent activity in defect) and size, circumferential profiles through the center of the defects were calculated from FBP and attenuation-corrected short-axis images (Fig. 4C). The defect severity in the heart wall of the chest phantom did not change significantly as a function of position and was not significantly different between the FBP and attenuation-corrected images. To estimate defect size, the defect profiles were fitted assuming a Guassian distribution and the FWHM values in Table 1 were obtained. From these data, defect size did not differ appreciably between the FBP and attenuation-corrected profiles with the exception of the posterior positioned defect. The resolution of the posterior defect improved with attenuation. The apparent decreased defect resolution for the posterior and septal positioned defects is due to the spatial depth variant resolution inherent in SPECT imaging.

In Figure 5, midventricular FBP and attenuation-corrected short-axis slices are shown for a 38-yr-old normal male volunteer (90 kg, body outline: 41 × 31 cm (major and minor axes diameters), 53% truncation of transmission image). Averaging the profile data acquired from the ten normal volunteers, tracer distributions for the FBP and attenuation-corrected cases were calculated and are displayed in the segmented polar map format (Fig. 6). In the polar maps of Figure 6, the rings of the heart proximal to the apex have been further segmented into apical and basal bands where the short-axis slices used in generating the maps were evenly divided between the two bands. For a basal short-axis slice, the lateral-to-posterior activity ratio improved from 1.17 ± 0.12 for FBP to 1.01 ± 0.07 for attenuation correction ($p = 0.009$, paired t-test). Basal attenuation appeared properly compensated as the peak basal-to-apical slice activity gradient along the posterior-inferior wall changed from 1.15 ± 0.12 for FBP to 1.01 ± 0.09 for attenuation-corrected ($p = 0.0002$, paired t-test). These values demonstrate the increased homogeneity in attenuation-corrected myocardial activity compared to FBP. In addition, the attenuation-corrected images displayed decreased tracer activity at the apex. This is consistent with

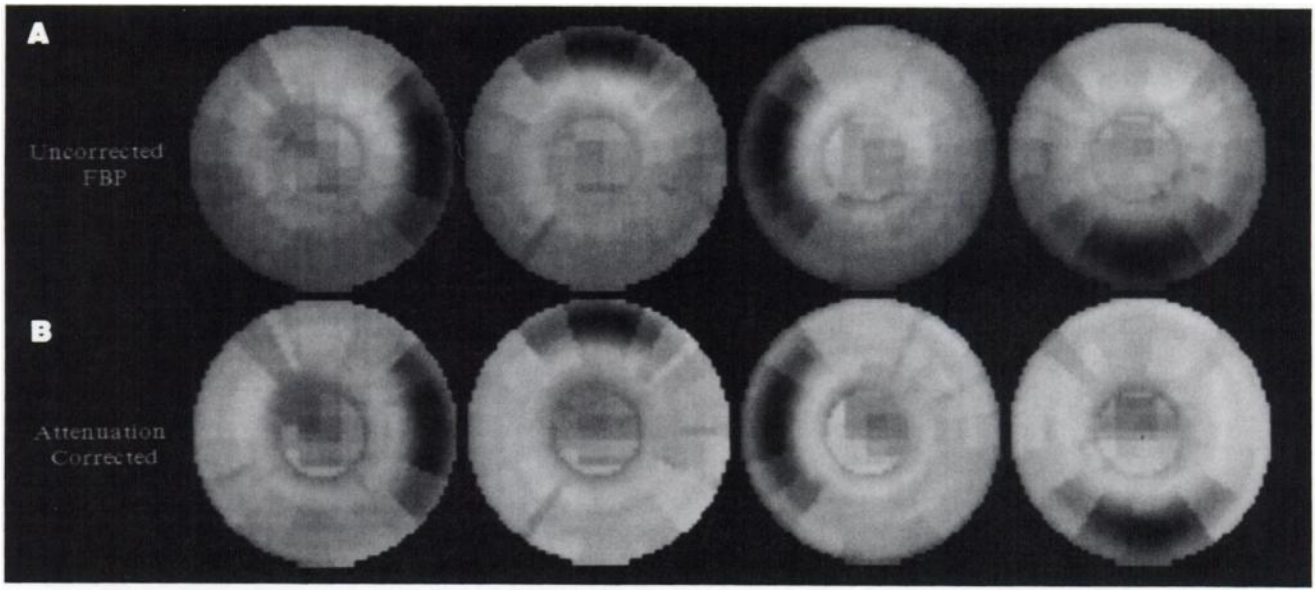

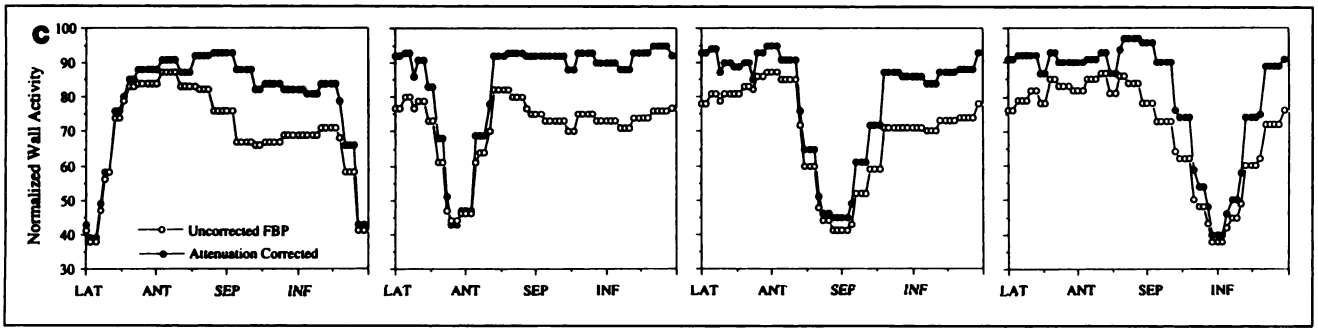

FIGURE 4. Uncorrected (A) and attenuation-corrected (B) polar map activity distributions of a heart phantom with a 2-cm × 45° cold defect. Normalized circumferential profiles through the defect are provided in (C).

anatomical apical thinning and the known partial volume effect inherent in SPECT imaging.

To illustrate the effect of attenuation correction on female breast-related artifacts, Figure 7 shows the short-axis slices from a 58-yr-old woman with large breasts (73 kg, body outline: 40 × 28 cm, 46% truncation of transmission image). Angiography had demonstrated a normal left coronary artery and a 70% stenosis of the proximal right coronary artery. From the FBP circumferential profile, there was a 16% reduction in anterior wall activity which was classified as a possible defect. The attenuation-corrected profile compensated for this breast attenuation and removed the depression in anteroseptal wall activity consistent with a normal left coronary artery.

TABLE 1
Defect Profile Fitting

Defect position	FWHM	
	FBP	Attenuation correction
Anterior	52°	50°
Lateral	54°	55°
Posterior	90°	75°
Septal	85°	82°

The stress short-axis slices from a 61-yr-old woman (70 kg, body outline: 40 × 28 cm, 46% truncation of transmission image) with anterior and basal-inferior defects are shown in Figure 8. A comparison of the corresponding FBP and attenuation-corrected circumferential profiles demonstrated little difference in the severity of the anterior defect. The increased severity (+13%) and extent of the inferior segment defect in the FBP slice compared to the attenuation-corrected slice was likely due to depression of perfusion tracer activity resulting from photon attenuation.

Figures 9–11 demonstrate the effects of attenuation correction on defects in and around the inferior wall. Figure 9 shows the stress short-axis slices of a 57-yr-old man (60 kg, body outline: 40 × 27 cm, 43% truncation of transmission image) with a severe inferolateral defect. For this patient, correcting for photon attenuation reduced defect severity from 29% of peak for FBP to 43% of peak for attenuation-corrected. Whereas defect severity diminished, defect definition improved. In Figure 10, stress short-axis slices are shown for a 57-yr-old man (70 kg, body outline: 40 × 29 cm, 48% truncation of transmission image) with a

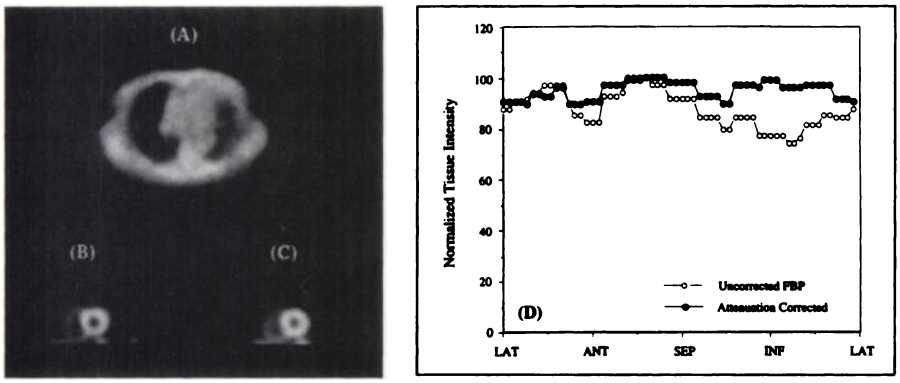

FIGURE 5. Normal volunteer. Uncorrected (B) and attenuation-corrected (C), midventricular short-axis slices from a 38-yr-old man (90 kg). Normalized circumferential profiles from these slices are depicted in (D). The reconstructed attenuation map used to correct the emission data for photon attenuation is displayed in (A).

defect involving the inferior wall. For this patient, the peak defect severity decreased from 52% in the FBP slice to 73% in the attenuation-corrected slice, representing a compensation of 21% in the inferior wall due to attenuation-correction. In addition, the extent of the defect was reduced from 102° for FBP to 78° for the attenuation-corrected profile. In Figure 11, the stress short-axis slices are shown for a 52-yr-old man (82 kg, body outline: 40 × 30 cm, 52% truncation of transmission image). Comparison of the FBP images to a normal, male polar map suggested an inferior defect. Visual and circumferential profile analysis of the attenuation-corrected slices, however, did not show this defect. Angiography confirmed the attenuation-corrected tracer distribution. The patient had undergone balloon angioplasty of the right coronary artery 3 days prior to the ^{201}Tl perfusion study and was left with only a 20%–30% residual coronary stenosis.

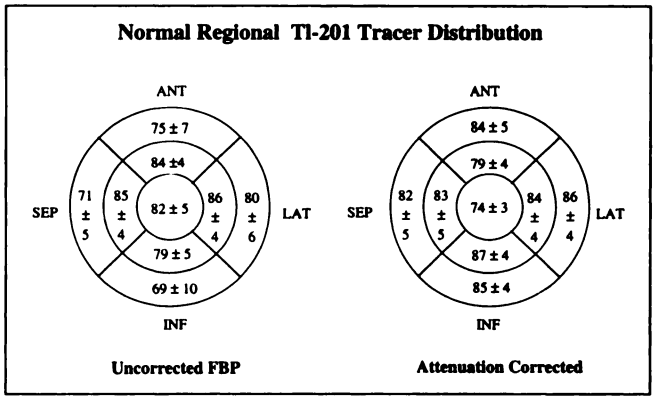

FIGURE 6. Average myocardial ^{201}Tl tracer polar map distributions from ten normal volunteers. The attenuation-corrected distribution shows improved tracer homogeneity compared to the uncorrected distribution. The maps were normalized to the percent maximal activity in the heart wall.

DISCUSSION

By using a triple-detector SPECT system equipped with an ^{241}Am line source, anatomic and physiologic tomographic data can be measured simultaneously. The concurrent measurements do not increase patient imaging time and eliminate the need for spatial registration of image sets acquired separately. The attenuation-corrected images from the healthy volunteers showed excellent uniformity in tracer distribution in the myocardium similar to normal ^{82}Rb and ^{62}Cu PTSM tracer distributions seen routinely in PET (*22,23*). As a result, the dependence of tracer distribution on patient size and density was significantly diminished. This behavior should eliminate the need for gender-specific normal databases (*24*), render obsolete many of the rules adopted to compensate for attenuation artifacts (*25–29*) and permit narrower defect thresholds to be applied for identifying regions of hypoperfusion. These benefits should translate into increases in sensitivity and specificity for ^{201}Tl perfusion tomography as compared to

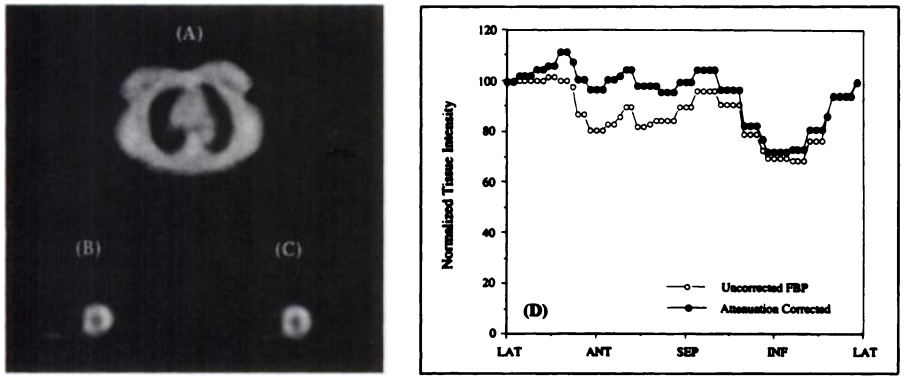

FIGURE 7. A woman with a breast attenuation artifact. Uncorrected (B) and attenuation corrected (C), midventricular short-axis slices from a 58-yr-old woman (72 kg). The uncorrected FBP circumferential profile shows a 16% depression in activity in the anterior-septal region which appears normal in the attenuation-corrected profile. The reconstructed attenuation map used to correct the emission data for photon attenuation is displayed in (A).

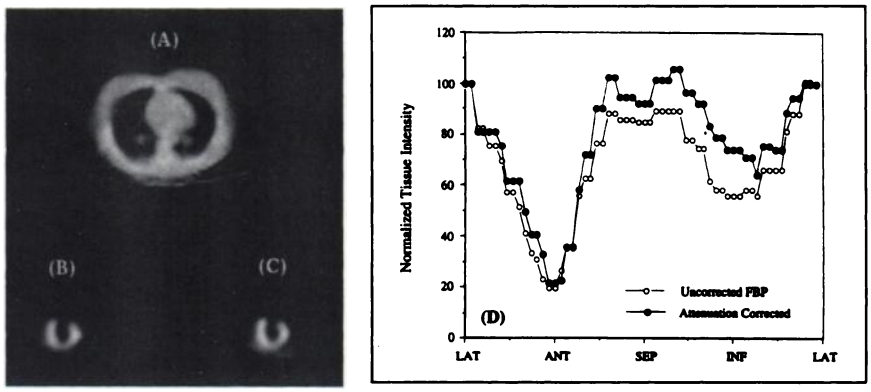

FIGURE 8. A woman with fixed anterior and inferior lesions. Uncorrected (B) and attenuation-corrected (C), midventricular short-axis slices from a 61-yr-old female (70 kg). The severity and extent of the anterior defect did not significantly change after correcting for photon attenuation as seen in the circumferential profiles (D). In the inferior defect, attenuation correction reduced the severity by 13%. The reconstructed attenuation map used to correct the emission data for photon attenuation is displayed in (A).

previously reported studies that did not use attenuation-correction (*30–34*).

Circumferential profile analysis on stress short-axis slices from five patients demonstrated: (a) proper correction for breast (Fig. 7) and diaphragmatic (Fig. 11) attenuation, (b) no significant difference in defect severity or extent between FBP and attenuation-corrected slices having anterior or lateral defects (Fig. 8) and (c) significant decreases in attenuation-corrected defect severity (20%–30%) and extent compared to FBP for patients with defects in the inferior-posterior wall (Figs. 9 and 10). Results from the remaining 35 patients not illustrated in this paper were consistent with these findings.

As previously described, the primary disadvantage of line source fanbeam TCT geometry is the truncation of transmission data. The degree of truncation depends on the camera orbit radius and the focal length of the collimator. For the phantom study, the orbit radius (center of rotation-to-collimator face) was 21.7 cm which provided a nontruncated transmission imaging FOV of 25.1 cm. Approximately 21% of the phantom area is truncated by this geometry when the elliptical dimensions of the chest phantom (31 × 23 cm) are used. From Figure 2, it is evident that our transmission algorithm handles this amount of truncation quite well.

For the patient studies, the average orbit radius was

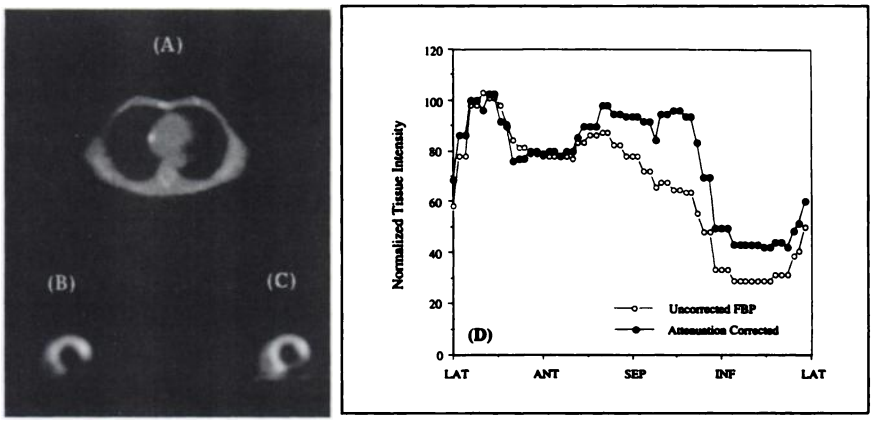

FIGURE 9. A man with fixed inferolateral defect. Uncorrected (B) and attenuation-corrected (C), midventricular short-axis slices from a 57-yr-old man (60 kg). Circumferential profile analysis (D) showed a reduction in defect severity of 14% after correction for photon attenuation. The reconstructed attenuation map used to correct the emission data for photon attenuation is displayed in (A).

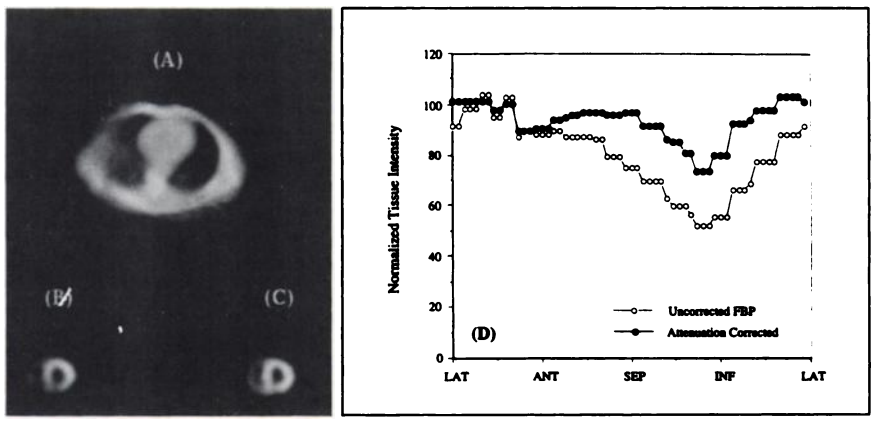

FIGURE 10. A man with fixed inferoseptal defect. Uncorrected (B) and attenuation-corrected (C), midventricular short-axis slices from a 57-yr-old male (70 kg). Circumferential profile analysis (D) showed a reduction in defect severity of 21% after correction for photon attenuation. The reconstructed attenuation map used to correct the emission data for photon attenuation is displayed in (A).

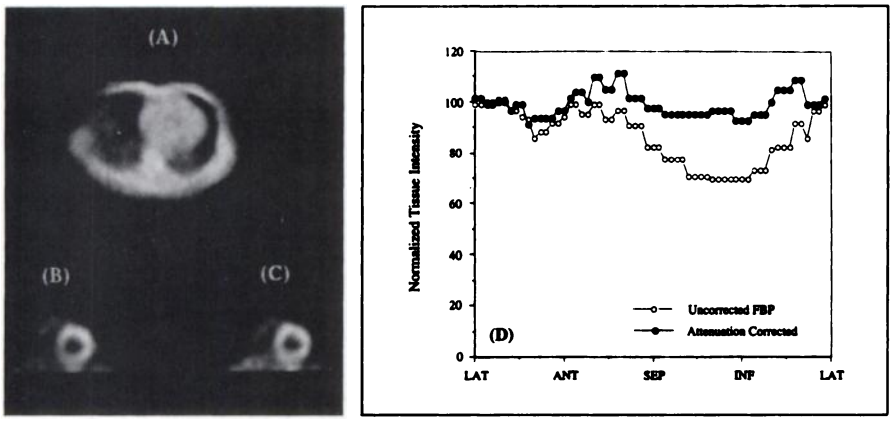

FIGURE 11. Male patient with inferior wall attenuation artifact. Uncorrected (B) and attenuation-corrected (C), midventricular short-axis slices from a 52-yr-old man (82 kg). There is 23% depression in tracer activity in the inferior wall of the uncorrected FBP image compared to the normal tracer level in the corrected image (D). Angiographic data supported the attenuation-corrected images. The reconstructed attenuation map used to correct the emission data for photon attenuation is displayed in (A).

23 ± 1.1 cm. This radius provides an untruncated transmission FOV diameter of 24.4 cm. The average elliptical support for the body outline used for the patient studies was (40 ± 2) cm × (30 ± 3) cm. Based on these dimensions, the average patient torso area was truncated by approximately 50%. To assess the ability of our transmission algorithm, we performed TCT with a 5.55 GBq ^{241}Am transmission line source on an 80-kg male volunteer with a chest circumference of 107 cm (width 40 cm, depth 26 cm), who was imaged using a 65-cm focal length centered fanbeam collimator (PRISM 3000 System) and with a 55.5 cm focal length collimator with its focal line offset by 16.1 cm (MULTISPECT III, Siemens Medical Systems, Hoffman Estates, IL). The reconstructed images are displayed in Figure 12. Row (A) shows the FBP images from the centered fanbeam collimator. The bright ring artifact depicts the nontruncated transmission FOV. The images in row (C) are FBP reconstructions of the offset fanbeam collimator data. This projection dataset was essentially untruncated and provides reference images for comparison. The images in row (B) were reconstructed from the centered fanbeam collimator by minimizing equation (1) and using an elliptical support of 41 × 29 cm for the body outline. From a qualitative comparison, the iteratively reconstructed (truncated) images in row B agree well with the FBP untruncated images in row C. There is, however, some distortion evident in the iteratively reconstructed images, most noticeably at the lung-tissue boundaries (i.e., image 3 in row B) resulting from data truncation. Quantitatively, there were no significant differences in regional attenuation coefficients (right lung: 0.0593 ± 0.013/cm versus 0.0575 ± 0.015/cm, tissue: 0.206 ± 0.010/cm versus 0.210 ± 0.011/cm, bone was not delineated) between the images of rows B and C.

Based on the images presented in Figure 12 and visual examination of the attenuation maps from the 50 subjects imaged, we believe that the transmission algorithm based on minimizing the objective function defined by Equation 1 provides accurate attenuation maps when the degree of truncation is less than 50%. The quality of the attenuation maps shown in Figures 2, 5, 7–9 and 12 confirm this statement. For large patients with greater than 50% truncation

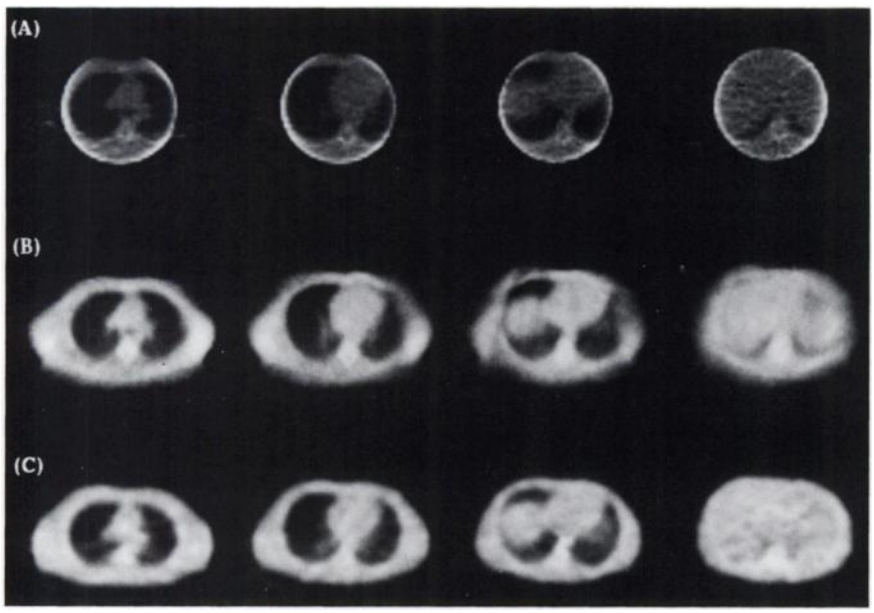

FIGURE 12. Attenuation map images of a male chest. Images in row (A) were reconstructed from truncated transmission data using FBP, while the images in row (B) were iteratively reconstructed from the same truncated dataset. The images in row (C) were reconstructed from untruncated transmission data using FBP. The iteratively reconstructed truncated images (B) agree well with the untruncated images (C) with some slight distortions evident near the lung-tissue boundary of the truncated images. There were no significant differences in the attenuation coefficients between images of rows B and C.

in their transmission data, however, truncation data losses can result in undefined or unrealistically dense body wall tissue. An example of this type of artifact is seen in Figures 10 and 11, where the right lateral body wall is not well defined or is absent in some areas. For these patients, we recommend the use of a longer focus collimator (e.g., 110 cm) or a line source with a fanbeam collimator with an offset focus. Patient size can be assessed easily prior to imaging and geometric requirements can be determined. We believe that this procedure is less time-consuming than sequential TCT/SPECT imaging and does not pose the problem of misregistration between the TCT and SPECT data.

Although the imaging and processing methods presented in this work correct for absorptive losses in the body, they do not compensate for photon scatter in the body, which degrade defect resolution and prohibits absolute quantification of tracer uptake. Based on the homogeneity of the tracer uptake of ^{201}Tl in normal volunteers and the close agreement of this distribution with published ^{82}Rb and ^{62}Cu-PTSM distributions of PET, we hypothesize that scatter did not significantly affect our normal database maps. Because defect contrast is degraded by scattered photons which can have a significant effect on the efficacy of the study, we are currently implementing and validating various multi-energy window scatter correction methods (*35,36*) with our current imaging and processing protocol to address photon scatter.

The variation of defect resolution as a function of defect position (Fig. 4C) illustrates the necessity for compensation for the variation in the geometric point response function as a function of distance. The geometric point response function can be modeled directly in the system matrix **A** in the objective function of Equation 3. Preliminary results from one-dimensional modeling improved defect resolution and decreased variation with defect position. The additional modeling increased computation time from 2 to 4 min for 18 slices, and the memory requirements for the system matrix **A** increased from 4 Mbytes to 9 Mbytes for a 64 × 64 × 60 acquisition, but further validation is required.

CONCLUSION

A triple-detector SPECT imaging system fitted with an ^{241}Am line source and a fanbeam collimator was used to demonstrate that transmission-emission tomography is achievable in the clinic with acquisition and processing stages each taking less than 20 min. With this process, attenuation artifacts were effectively eliminated from the reconstructed emission images, yielding more accurate physiologic and anatomic information of the myocardium, including regional myocardial activity ratios and heart-to-lung activity ratios. With improved information, guidelines for diagnosing coronary heart disease in the presence of photon attenuation currently in use will need to be redefined. Based on these results, we anticipate improved specificity for myocardial perfusion SPECT when attenuation correction is applied. Prospective clinical validation in large patient populations is necessary to define the diagnostic benefit of attenuation correction for qualitative and quantitative analyses of cardiac SPECT for the detection of coronary heart disease.

ACKNOWLEDGMENTS

The authors thank Steven Pitt, Anthony Harris and Lisa Cotton for their help in data acquisition and processing. This work was supported by National Cancer Institute grant CA09015 and National Institutes of Health grants RO1 HL41047 (MS), RO1 CA32846 (WLR) and R29 CA60711 (JAF). This work was completed during the tenure of an Established Investigatorship from the American Heart Association (MS).

REFERENCES

1. Chang LT. A method for attenuation correction in radionuclide computed tomography. *IEEE Trans Nucl Sci* 1978;25:638–643.
2. Kuhl DE, Hale J, Eaton WL. Transmission scanning: a useful adjunct to conventional emission scanning for accurately keying isotope deposition to radiographic anatomy. *Radiology* 1966;87:278–284.
3. Malko JA, Gullberg GT, Kowalsky WP, Van Heertum RL. A count-based algorithm for attenuation-corrected volume determination using data from an external flood source. *J Nucl Med* 1985;26:194–200.
4. Malko JA, Van Heertum RL, Gullberg GT, Kowalsky WP. SPECT liver imaging using an iterative attenuation correction algorithm and an external flood source. *J Nucl Med* 1986;27:701–705.
5. Tsui BM, Gullberg GT, Edgerton ER, et al. Correction of nonuniform attenuation in cardiac SPECT imaging. *J Nucl Med* 1989;30:497–507.
6. Bailey DL, Hutton BF, Walker PJ. Improved SPECT using simultaneous emission and transmission tomography. *J Nucl Med* 1987;28:844–851.
7. Frey EC, Tsui BM, Perry JR. Simultaneous acquisition of emission and transmission data for improved Tl-201 cardiac SPECT imaging using a Tc-99m transmission source. *J Nucl Med* 1992;33:2238–2245.
8. Manglos SH, Bassano DA, Thomas FD. Cone-beam transmission computed tomography for nonuniform attenuation compensation of SPECT images. *J Nucl Med* 1991;32:1813–1820.
9. Manglos SH, Bassano DA, Thomas FD, Grossman ZD. Imaging of the human torso using cone-beam transmission CT implemented on a rotating gamma camera. *J Nucl Med* 1992;33:150–156.
10. Lang TF, Hasegawa BH, Liew SC, et al. Description of a prototype emission-transmission computed tomography, imaging system. *J Nucl Med* 1992;33:1881–1887.
11. Tung C-H, Gullberg GL, Zeng GL, Christian PE, Datz FL, Morgan HT. Non-uniform attenuation correction using simultaneous transmission and emission converging tomography. *IEEE Trans Nucl Sci* 1992;39:1134–1143.
12. Jaszczak RJ, Gilland DR, Hanson MW, Jang S, Greer KL, Coleman RE. Fast transmission CT for determining attenuation maps using collimated line source, rotatable air-copper-lead attenuators and fan-beam collimation. *J Nucl Med* 1993;34:1577–1586.
13. Tan P, Bailey DL, Meikle SR, Eberl S, Fulton RR, Hutton BF. A scanning line source for simultaneous emission and transmission measurements in SPECT. *J Nucl Med* 1993;34:1752–1760.
14. Ficaro EP, Fessler JA, Rogers WL, Schwaiger M. Comparison of Am-241 and Tc-99m as transmission source for the attenuation correction of Tl-201 SPECT imaging of the heart [Abstract]. *J Nucl Med* 1994;35:652–663.
15. Ficaro EP, Hawman EG, Schwaiger M. Simultaneous transmission/emission tomography using a line source with an off-center fanbeam collimator [Abstract]. *J Nucl Med* 1994;35 (suppl):191p.
16. Manglos SH, Gagne GM, Bassano DA. Quantitative analysis of image truncation in focal-beam CT. *Phys Med Biol* 1993;38:1443–1457.
17. Ficaro EP, Fessler JA. Iterative reconstruction of truncated fan beam transmission data. 1993 IEEE *Nuc Sci Sym Abstracts* 1993:143.
18. Sauer K, Bouman C. A local update strategy for iterative reconstruction from projections. *IEEE Trans Signal Proc* 1993;41:523–548.
19. Fessler JA. Penalized weighted least-squares image reconstruction for positron emission tomography. *IEEE Trans Med Imaging* 1994: in press.
20. Hubbell JH. Photon cross sections, attenuation coefficients and energy absorption coefficients from 10 keV to 100 GeV. *NSRDS-NBS* 1969;29:64.

21. Garcia E, Van Train K, Maddahi J, et al. Quantification of rotational thallium-201 myocardial tomography. *J Nucl Med* 1985;26:17–26.
22. Schwaiger M, Muzik O. Assessment of myocardial perfusion by positron emission tomography. *Am J Cardiol* 1991;67:35D–43D.
23. Beanlands RS, Muzik O, Hutchins GD, Wolfe Jr ER, Schwaiger M. Heterogeneity of regional nitrogen-13-labeled ammonia tracer distribution in the normal heart: comparison with rubidium-82 and copper-62-labeled PTSM. *J Nucl Cardiol* 1994;1:225–235.
24. Eisner R, Tamas M, Clononger K, et al. Normal SPECT thallium-201 bull's-eye display: gender differences. *J Nucl Med* 1988;29:1901–1909.
25. Rehn T, Griffith LS, Achuff SC, et al. The inconsistent pattern of thallium defects: a clue to the false-positive perfusion scintigram. *Am J Cardiol* 1981;48:224–232.
26. DePuey EG, Garcia EV. Optimal specificity of thallium-201 SPECT through recognition of imaging artifacts. *J Nucl Med* 1989;30:441–449.
27. DePuey EG, Garcia EV. Prone versus supine thallium myocardial SPECT: a method to decrease artifactual inferior wall defects. *J Nucl Med* 1989;30: 548–555.
28. Tamaki N, Yonekura Y, Kadota K, Kambara H, Torizuka K. Appearance of breast attenuation artifacts with thallium myocardial SPECT imaging. *Clin Nucl Med* 1985;10:694–696.
29. Beller GA. Diagnostic accuracy of thallium-201 myocardial perfusion imaging. *Circulation* 1991;84(suppl 3):I1–I6.
30. Borges-Neto S, Mahmarian JJ, Jain A, Roberts R, Verani MS. Quantitative thallium-201 single photon emission computed tomography after oral dipyridamole for assessing the presence, anatomic location and severity of coronary artery disease. *J Am Coll Cardiol* 1988;11:962–969.
31. Nguyen T, Heo J, Ogibly D, et al. Single-photon emission tomography with thallium-201 during adenosine-induced coronary hyperemia: correlation with coronary arteriography, exercise thallium imaging and two-dimensional echocardiography. *J Am Coll Cardiol* 1990;16:1375–1383.
32. Dondi M, Monetti N, Leverato M, et al. Diagnostic accuracy of single-photon emission computed tomography with thallium-201 for the identification of diseased coronary arteries. *J Nucl Allied Sci* 1990;34:19–23.
33. Nishimura S, Mahmarian JJ, Boyce Tm, Verani MS. Quantitative thallium-201 single photon emission computed tomography during maximal coronary vasodilation with adenosine for assessing coronary artery disease. *J Am Coll Cardiol* 1991;18:736–745.
34. Allman KC, Berry J, Sucharski LA, et al. Determination of extent and location of coronary artery disease in patients without prior myocardial infarction by thallium-201 tomography with pharmacologic stress. *J Nucl Med* 1992;33:2067–2073.
35. Koral KF, Swailem FM, Clinthorne NH, Rogers WL, Tsui BMW. Dual-window Comptom-scatter correction in phantoms: errors and mulitpleir dependence on energy. *J Nucl Med* 1990;31:798–799.
36. Wang X, Koral KF. A regularized deconvolution-fitting method for Compton-scatter correction in SPECT. *IEEE Trans Med Imaging* 1992;11:351–360.